Optical Creation of a Supercrystal with Three-Dimensional Nanoscale Periodicity

V.A. Stoica[1], N. Laanait[2], C. Dai,[1] Z. Hong[1], Y. Yuan[1], Z. Zhang[3], S. Lei[1], M.R. McCarter[4], A. Yadav[4], A. R. Damodaran[4], S. Das[4], G.A. Stone[1], J. Karapetrova[3], D.A. Walko[3], X. Zhang[3], L. W. Martin[4,5], R. Ramesh[4,5], L.-Q. Chen[1], H. Wen[3], V. Gopalan[1,*], and J.W. Freeland[3,*]

[1]Department of Materials Science and Engineering, Pennsylvania State University, University Park, Pennsylvania 16802, USA

[2]Center for Nanophase Materials Sciences, Oak Ridge, Tennessee 37831, USA

[3]Advanced Photon Source, Argonne National Laboratory, Argonne, Illinois 60439, USA

[4]Department of Materials Science and Engineering, University of California, Berkeley, CA 94720, USA

[5]Materials Sciences Division, Lawrence Berkeley National Laboratory, Berkeley, CA 94720, USA

*Corresponding authors: vxg8@psu.edu, freeland@anl.gov

Abstract

Stimulation with ultrafast light pulses is a means to realize and manipulate new states of matter. While non-equilibrium optical excitations can lead to transient phases with emergent structural, electronic, and magnetic phenomena, a significant challenge is to stabilize them as persistent states. Here, we show that atomic scale $PbTiO_3/SrTiO_3$ superlattices that delicately counterpoise strain and polarization states in alternate layers, undergo a light-stimulated transition to a new polar supercrystal phase, which is triggered by sub-picosecond excitation with above bandgap energy light. The resulting supercrystal persists indefinitely under ambient conditions, has not been created via equilibrium routes, and can be erased by heating above a critical temperature. Using X-ray scattering and microscopy, we reveal that this unusual and complex phase consists of long-range, coherent three-dimensional (3-D) structure with nanoscale periodicities of up to 30 nm, consisting of polar, strain, and charge cooperative ordering. By only adjusting dielectric properties, the phase-field model describes this emergent phase as a photo-induced charge-stabilized supercrystal that is triggered from a mixed two-phase thermal equilibrium state. Our results demonstrate new opportunities for light activated pathways to thermally inaccessible and emergent metastable states.

The structural and functional complexity of artificial nanomaterials challenges the frontiers of experimental capability, calling for novel approaches to materials synthesis. During the last few decades, a new class of "non-equilibrium photo-induced materials", which exist only in the transient state, has emerged under ultrafast-optical excitation. While in the vast majority of cases, either electronic, magnetic, or structural orders undergo prompt collapse into disorder [1-3], in a few other cases, novel orders have been stabilized, such as a switch of the order parameter in the magnetic compounds [4] and the creation of new condensates such as superconductors [5], charge/spin density waves [6,7] and amorphous-to-crystalline transformations [8]. More recently, new phases not present in an equilibrium thermodynamic phase diagram have arisen out of the non-equilibrium optical excitation either as transient [9,10] or persistent [11,12] states. Such thermally inaccessible states are both of fundamental interest, as they offer a unique window into a regime of strong coupling between microscopic degrees of freedom in a material, and could possess novel functionalities not present in equilibrium states. However, irrespective of the physical nature of the excited state or the equilibrium parent phase, a key challenge remains, namely the conversion of the transient states into new persistent phases at room-temperature.

A central idea exploited in this work is to counterpoise distinct order parameters in an atomic-scale heterostructure so as to produce a ground state that is very susceptible to external perturbations such as fields and light. In particular, we explore $(PbTiO_3)_n/(SrTiO_3)_n$ superlattices (PTO/STO SLs), where there is a subtle balance between the polarization (Landau), electric, gradient, and elastic energies. The energetics of these heterostructures is dictated by interlayer coupling through electrostatic as well as elastic strain gradients, producing confinement and proximity of competing phases [13-17]. When this system is grown on $DyScO_3$ substrates, the $SrTiO_3$ is under tensile strain, which induces an in-plane polarization, and $PbTiO_3$ is under

compression, which favors out-of-plane polarization. However, this leads to highly charged interfaces; to avoid it, the system devolves into a two-phase mixture of ferroelectric-ferroelastic a_1/a_2 domains (FE) and polarization vortices (V) in the as-grown samples[15,16].

Starting from this two-phase mixture, here we show that by using an ultrafast optical pulse, we can manipulate the electrostatic landscape and enable the formation of a stable structure with long-range nanoscale polar order consisting of polar vortices that are intertwined in three-dimensions. The process of creating this persistent structure, which we refer to as a supercrystal (S) phase, is possible with sub-picosecond optical pulse excitation with light above the bandgap. By tuning of the dielectric constant parameter, phase field modelling reproduces the observed supercrystal phase and associates its formation to the screening of optically generated free carriers at the interfaces. In addition, the model self-consistently predicts a thermal erase process in agreement with experiments.

The creation of the S-phase from a phase mixture of FE and V phases is summarized in **Figure 1**. The 3-D depiction of the phases is extracted from a phenomenological phase-field model (Methods), where the starting two-phase mixture in the as-grown heterostructure shown in **Fig. 1a** has been confirmed by a multitude of experimental observations on PTO/STO SLs[16]. Using sub-picosecond optical pulses, this FE- and V-phases can be converted into the S-phase (see **Fig. 1b**). These phases were experimentally mapped using X-ray scattering and structural imaging with area detectors (see **Fig. 1c**) to characterize the initial and photoinduced S-phase in $n = 16$ superlattices. The results show a collapse of the mixed phase with two superlattice peaks corresponding to regions of FE and V that convert post-excitation to a single S-phase superlattice peak (see **Fig. 1d**). The coherent ordering of the S-phase stems from its polar nature as well as the interaction with optical pulses and represents a hidden order that is not present in the equilibrium phase

diagram. Thermal annealing, however, can be used to erase the S-phase and convert back to the starting two-phase mixture.

Next, we determine the detailed structure of the S-phase using X-ray diffraction and microscopy. **Figures 2a**,**b** depicts the reciprocal space scans in the K-L reciprocal plane, corresponding to the *y*-*z* plane in real space, where the *y* and *z* axes are aligned with the [-110] and [110] of the DSO substrate, respectively. In the pristine state, the distinct out-of-plane lattice constant of the FE and V phases coexist to give rise to two independent superlattice reflections along the [00L] as labeled in **Fig. 2a** [16]. Upon optical excitation above a critical fluence using ~900 fs pulses with 400 nm wavelength light, the two-phase mixture transforms into the S-phase possessing long-range 3-D coherent arrangement of polarization, strain, and charge in an orthorhombic supercell size of ≈ 11 x 30 x 25 nm^3. Accordingly, the two superlattice reflections of the pristine state collapse into a single vertical superlattice reflection (**Fig. 2b**)**,** with the simultaneous appearance of strong peaks in the off-specular part of the spectrum resulting from a fully coherent 3-D modulation of the lattice with well-defined periodicity of ≈ 30 nm x 25 nm in the *y*-*z* plane. The reciprocal space cuts along the H-K and H-L planes show this phase is fully 3-D ordered (Supplementary material **Fig. S1**)**. Figure 2c** shows the X-ray diffraction microscopy (XDM) map of the strain in the (103) lattice planes obtained from full-field Bragg imaging [18,19], which reveals that in their pristine FE+V state, the FE and V domains have a quasi-periodic stripe pattern with ≈ 350 nm periodicity in the plane of the PTO layer, which is in agreement with piezoresponse force microscopy [16]. A third periodicity of 11 nm, characteristic of the V ordering in the pristine samples [14-16], also appears along the *x* direction (*i.e.*, the [001] of the DSO substrate as shown in **Supplementary Materials**, **Figs. S1-2**).

After light irradiation, the FE and V phases are erased and a new uniform S phase is formed. In the S phase, the strong mesoscale strain modulations characteristic of the FE+V-phase mixture, are replaced by a uniform strain state (**Fig. 2d**) as probed by XDM. Note that the S-phase structural modulations occurring on a length scale of < 30 nm are below the real space XDM resolution of 60 nm. Concomitant with the formation of a uniform strain state for the S-phase, the structural coherency is greatly enhanced, which can be seen by the formation of Laue fringes between satellites (**Fig. 2b**). In addition, the in-plane diffraction shows the formation of a strain state that is in direct registry with the substrate and persists throughout the entire superlattice (see details in the **Supplementary Material, Fig. S3**). This finding represents a highly unusual case where light irradiation of the sample greatly enhances the long-range strain coherency when it is assisted by spatially modulated polar displacements on the nanoscale. Second-harmonic generation and PFM measurements support that the S phase is polar (**Supplementary Material, Fig. S4**). Attempts to resolve the atomic structure with high-resolution transmission electron microscopy (TEM) have not been successful to date due to the instability of the S-phase during TEM specimen preparation.

To understand the formation process of the S phase, we explored in detail the characteristics of the response to the nature of ultrafast excitation. The first observation is that it requires direct carrier excitation above the bandgap [20] of the PTO layer with 400 nm light, while excitations below the bandgap do not result in S-phase formation. Furthermore, the S-phase formation is only obtained by optical-pulse irradiation above a critical laser fluence (**Fig. 3a)**. In addition, the threshold was found to systematically increase with pulse duration (**Fig. 3b**). These results are consistent with a critical peak photo-carrier density for transformation that needs to be created before the time it takes carriers to relax via other channels.

Additional support for a non-equilibrium electronic process is shown in the temperature dependence of the S-phase. While we have seen that under ambient conditions the S-phase is stable for at least a year, heating experiments show that the S-phase is stable up to a temperature of ~ 430 K and disappears at a critical temperature of $T_S \approx 470$ K (**Fig. 3c**). After exceeding T_S, the sample exists in the pure FE phase and then returns to a mixture of FE+V phases upon cooling (**Supplementary Material, Fig. S5-6**). Given this result, any ultrafast heating would serve to only destabilize the S-phase and not create it. In addition, the write/erase process is entirely repeatable and the S-phase has been successfully written and erased multiple times on several different samples, which suggests that it is unambiguously connected with intrinsic physical processes in the superlattice. For both the write and erase process, there is a sharp transition where ordering or disordering of the S-phase occurs when a threshold value for the control parameter is reached.

To study the S-phase formation, we consider first how these observations fit within the current understanding of polar heterostructures. Prior ultrafast optical-excitation studies of PTO nanolayers [21] and superlattices [22] have observed lattice dynamics due optically generated carriers that segregate to the surface/interface and result in a reduction of the depolarizing field via charge-carrier screening, but no conversion to a new polar state was observed. For the case of PTO/STO superlattices, an additional factor is the band-bending at the PTO/STO boundary [23,24] which can lead photo-induce carriers in STO to be trapped near the interface. It is known that photocarriers in STO cause a large increase in the dielectric constant [25] due to the formation of polarons [26], which is an additional source for screening the polar structure in PTO. From a view as a capacitor-like structure, where the strongly-polar PTO is sandwiched between dielectric STO layers with smaller relative polarizability, modifications of the vertical depolarizing electric field, $E_d \sim CP_z/\varepsilon_0\varepsilon_{PTO}$ [27,28] can occur both from charge carrier screening (C) and changes in the

relative dielectric permittivity, ε_{PTO}. For these reasons, in the modeling of the process we have focused on photocarrier driven reduction of depolarizing field as the primary modality.

To model the structure and creation of the S phase, we employ phase-field techniques [29], which have successfully predicted the co-existence of the pristine FE+V-phase mixture [14-16]. Here, we focus on altering the depolarizing field by accounting for its reduction by photocarrier screening. In this phenomenological model, the tuning of the depolarizing field is achieved by modifying a single material parameter, namely, the background dielectric constant, ε_b [15]. We note that the primary effect of changing ε_b is to mimic the charge-carrier screening of the local internal field while preserving the dielectric approximation of the phase-field models. In this way, the ε_b increase is assumed to incorporate possible contributions to the internal-field screening such as ionized impurities and free- or trapped-charge carriers. As noted above, the two-phase pristine state has been well described using ε_b values of ~10-20 [15,16]. By increasing ε_b, the energy for a polar displacement reorientation from in-plane to out-of-plane is reduced by generating bound charge accumulation at interfaces that compensates the local-polarization discontinuity. Moreover, above a critical value of $\varepsilon_b \approx 80$, there is a clear discontinuity in the total energy at the point where the S-phase emerges (**Fig. 4a,b**). During the S-phase transition, the electrical and gradient energies increase but the reduction of the elastic and Landau energy contributions move the system towards a new energy minimum. A similar interplay in the S-phase formation energetics is observed during the dynamic transition to the S-phase following a sudden increase of ε_b from 5 to 200 (**Fig. S7**). This nanoscale transformation of the polar order is characterized by an increase of the spatial average of the vertical-polarization component, P_z, which is correlated with the bound charge accumulated at interfaces and is quasi-linearly dependent on ε_b as shown in **Fig. 4c** (see also **Fig. S8a**). Furthermore, the gradual increase of ε_b is indeed reducing the depolarizing field at the

superlattice interfaces as expected (see **Fig. S8b**) that in turn allows the formation of structures with larger effective P_z. Accordingly, when $\varepsilon_b < 80$, the increase of average vertical-polarization component evolves by an increase of the V phase volume fraction at the expense of the FE phase. There is a clear boundary for $\varepsilon_b > 80$, where the FE-phase collapses and the S-phase is formed. To see how carrier relaxation would affect the S-phase stability after its formation, we also followed the phases formed as ε_b was decreased back to the starting value below the threshold and observed a significantly larger average P_z and the presence of a disordered S-phase.

These results confirm the key role for optically induced dielectric changes in altering the overall energy landscape, which in turn allows the persistent formation of ordered states that are not accessible otherwise. To connect the values of ε_b to the experimental conditions, we utilize both the observed and calculated strain to assign a value of ε_b corresponding to experimental pristine and converted phases. The ε_b value that produces a strain state that matches the experimental observations is ~ 20 (bound charge density of ~ 0.78 x 10^{19} cm^{-3}) for the pristine state and ~ 100 (bound charge density of ~ 5.5 x 10^{20} cm^{-3}) for the converted S-phase state, indicating a large enhancement for bound charge accumulation at interfaces.

To connect phase-field modeling with the observed structural modulations, we note that strong diffuse scattering is connected to the nanometer scale lattice modulations that are created at the atomic level by the direction of the polar distortions. To mimic this effect from the polar lattice as well as the charging of the structure, we further show the local polarization variation superimposed with the in-plane strain modulations throughout the 3-D structure (**Fig. 5a**) along with a map of bound charge distribution (**Fig. 5b and Fig. S9a**). The formation of polar nanoregions within the S-phase lead to lattice distortions in the y-z plane that match the symmetry of the X-ray diffraction by a Fast-Fourier transform of the model structure (**Fig. 2b**). Phase-field

modeling is then seen to reproduce the observed structural symmetry of the S-phase, suggesting a plausible mechanism for tuning the effect of internal field by which such a phase can emerge. For the ordering in the plane of the sample (**Fig. 5e and Fig. S9b-c**), we find arrays of intertwined polar vortices with both vertical and horizontal core axes orientations, in contrast to the V-phase which has vortex axes only in the plane of the PTO film layers. Further, unlike the V-phase, which only has local correlations within a single domain and very weak correlations vertically between layers, the vortices in the S phase are ordered in 3D. From the temperature dependent phase field results, the changes of the calculated bound charge density correlate well with the X-ray results (**Fig. 3c**). Overall, the observation of a dramatic phase transition from the FE+V to the S phase, which is optically induced in the experiments, shows consistency with the model regarding the essential aspects: symmetry and periodicities (**Fig. 2c**), existence of a critical threshold for conversion (**Fig. 4a**) as well as an enhanced thermal stability (**Fig. S10-12**).

We note that microscopic mechanisms consisting of ultrafast carriers and lattice dynamics ultimately underlying the supercrystal formation are not accessible via our phenomenological modeling and must be addressed in future work. Nonetheless, good agreement between experiments and phase-field modeling, in particular, in the latter's capability to reproduce the evolution of structural phases as a function of temperature without any additional parameter tuning (see Fig. 3c), gives strong support to a formation mechanism dominated by reduction of the depolarizing field via photocarrier excitation. By contrast to the photo-excitation of bulk crystals or crystalline thin-films that show no new phases, the creation of a polar supercrystal with a fs optical pulse highlights the special role of the superlattice geometry employed here, especially, in the local spatial confinement of the ferroelectric order parameter. With photocarrier excitation occurring primarily in the $PbTiO_3$ layer, the proximal unexcited "cold" $SrTiO_3$ interlayers can act

as nanoscale heat sinks to promptly spread out the competing thermal excitations, which may quench the optically-stimulated transient states by exploiting non-adiabatic conditions to develop of long-range order in a way that might not be accessible by equilibrium pathways. This understanding also highlights routes to stabilize these new polar phases via tuning of the boundary conditions through alteration of the dielectric spacer material or environmental conditions.

Our discovery of this supercrystal formation reveals that the coupling between the superlattice layers can be optically manipulated to promote enhanced elastic interactions via optical pulse triggering of an electric perturbation. In turn, we can access a new type of ordering that consists of interpenetrating polar vortices inside this long-range 3D ordered structure with nanoscale periodicity. This new phase captures and stores the light-activated carriers in a highly 3D charge ordered state, which could be a potential strategy for charge storage and highly tunable capacitors. More broadly, the idea of counterpoising other competing magnetic, charge and orbital states into heterostructures and perturbing them with light or fields could trigger electronic, orbital and magnetically ordered supercrystals with novel structures and functionalities.

Acknowledgements

V.A.S., Y.Y., L.W.M., Z.H., L-Q.C., H.W., V.G., and J.W.F. acknowledge support from the U.S. Department of Energy, Office of Science, Office of Basic Energy Sciences, under Award Number DE-SC-0012375 for the development of the materials and ultrafast experiments. Z.H. and C.D. acknowledge National Science Foundation Center for Nanoscale Science grant number DMR-1420620. Use of the Advanced Photon Source was supported by the US Department of Energy, Office of Science, under Contract No. DE-AC02-06CH11357. PFM data was collected at PSU, U. of California, Berkeley, and at the Center for Nanophase Materials Sciences, a DOE Office of Science User Facility at ORNL. NL acknowledges support from the Eugene P. Wigner Fellowship

at Oak Ridge National Laboratory (ORNL), a U.S. Department of Energy (DOE) facility managed by UT-Battelle, LLC for US DOE Office of Science under Contract No. DE-AC05-00OR22725. R.R and L.W.M. acknowledge funding from the Moore Foundation. V.A.S. would like to thank C.M. Schlepütz and J. Hammonds for their development of rsMap3D, valuable discussions with H. Zhou, S Kalinin, Q. Li, Y. Ren, J. Tischler and D.D. Fong, and C.A. Kurtz for technical support.

Methods section

Superlattice growth using RHEED-assisted pulsed laser deposition

Superlattices of $(PbTiO_3)_n/(SrTiO_3)_n$ were synthesized using reflection high-energy electron diffraction (RHEED)-assisted pulsed laser deposition with a KrF excimer laser. A buffer layer of ~2 unit cells $SrRuO_3$ was deposited on the $DyScO_3$ (110) substrates at a temperature and oxygen pressure of 700°C and 50 mTorr, respectively. Layers of $(PbTiO_3)_n/(SrTiO_3)_n$ (n = 16 unit cells) were grown at 620°C and 100 mTorr oxygen pressure. The intensity oscillations of the RHEED pattern were recorded throughout the deposition to monitor the layer-by-layer growth mode. The unit $(PbTiO_3)_n/(SrTiO_3)_n$ was repeated until the superlattice was about 100 nm thick (8 repeats). For all materials, the laser fluence was ~1.5 J/cm^2, and the repetition rate was 10 Hz. After growth, the superlattices were cooled to room temperature in 50 Torr of oxygen. The targets used for the deposition were a single crystalline $SrTiO_3$ target, a polycrystalline $SrRuO_3$ target, and a polycrystalline $Pb_{1.2}TiO_3$ target. A lead-rich target is necessary to deposit stoichiometric $PbTiO_3$.

Ultrafast laser setup

Optical excitation of superlattice was explored using femtosecond laser single pulses as well as pulse trains generated by a Ti:sapphire regenerative amplifier at 1 kHz. The duration of pulses, the total number of pulses, optical wavelength and laser fluence were all used for optical control of phase changes. The laser pulse duration was adjusted below 1 ps and measured using a single-shot autocorrelator. The laser

wavelength was adjusted to be either 400 nm or 800 nm at a laser fluence below 50 mJ/cm^2 to avoid damage. The use optical pulses longer than ~ 1ps results in spatially non-uniform phase conversion.

X-ray diffraction

X-ray diffraction (XRD) data was taken at the Advanced Photon Source using beamlines 7-ID-C, 11-ID-D, 33-BM, and 33-ID-B using a Pilatus area detector. XRD data was converted into the reciprocal space volumes using rsMap3D and cut along different directions to create different views of the data. The phase changes were monitored with XRD measurements of peaks and diffuse scattering satellites corresponding to in-plane periodic lattice modulations. Reciprocal lattice units from figures are in $2\pi/d_{hkl}$ Å^{-1}, where d_{hkl} is the lattice spacing for the hkl reflection. Pseudocubic lattice parameters relative to orthorhombic $DyScO_3$ substrate are shown in the following reference system: $[100]_{pc} \parallel [001]_o$ and $[010]_{pc} \parallel [-110]_o$.

Phase field simulations

In an attempt to simulate the polar structure change for the PTO/STO superlattice on a DSO substrate after the laser excitation, the phase-field simulation is performed. The evolution of the order parameter (spontaneous polarization vector) is obtained by solving the time-dependent Ginzburg-Landau (TDGL) equations:

$$\frac{\partial P_i(\vec{r},t)}{\partial t} = -L\frac{\delta F}{\delta P_i(\vec{r},t)}(i=1,2,3) \quad (1)$$

where L, r, and t denote the kinetic coefficient, spatial position vectors, and evolution time step, respectively. The total free energy F can be expressed by the volume integration of local Landau bulk, elastic/mechanical, electric/electrostatic, and gradient energy densities, *i.e.*,

$$F = \int (f_{Landau} + f_{Elastic} + f_{Electric} + f_{Gradient}) dV \quad (2)$$

All the material constants for $PbTiO_3$ and $SrTiO_3$ used in the simulations are adopted from previous reports (see main text, and [S4-S6]). A three-dimensional phase-field simulation of $(SrTiO_3)_{10}/(PbTiO_3)_{10}$ superlattices is performed using discrete grids of 200×200×250 with a grid spacing of 0.4 nm. The thickness of the substrate, film, and air are set as 30, 176, and 44 grids, respectively. Periodic boundary conditions are applied in both the *x* and *y* directions, and a superposition method is used along the *z* direction. Random noise (with a magnitude of <0.00001 C/m^2) is used as the initial setup to simulate the thermal fluctuation during the annealing process. The mechanical boundary condition is applied such that the out-of-plane stress is fully released on the top of the film, while the out-of-plane displacement is zero on the bottom of the substrate sufficiently far away from the substrate/film interface. Short-circuit electric boundary condition is used where the electric potential at the top film surface and the film/substrate interface is fixed to zero. A mixed phase coexistence of a_1/a_2-twin and vortex is first simulated as the initial structure (see main text) with the background dielectric constant set as 10. As shown in Fig. 1, the 3D structure is constructed by interconnecting of an a_1/a_2 twin region with normal ferroelectric/ferroelastic twins and a vortex region with continuous rotating polarization surrounding a vortex core. This structure is coherent with the experimental observations by piezoelectric force microscopy (PFM) and transmission electron microscopy (TEM) in the current PTO/STO system grown on a (110)o-$DyScO_3$ substrate at intermediate periodicities (n=10, 16).

After the laser excitation, it is assumed that the superlattice film is more conducting due to photo-carrier excitation. As a consequence, the background dielectric constant for the superlattice is then increased to 200 to model the decrease of the internal depolarization field after the laser excitation. The 3-dimensional complex hierarchical ladder-like supercrystal phase is formed with periodical vortex arrays separating by *a*-domains (shown in Figure 1), in good agreement with the experimental *X*-ray diffraction patterns.

Optical second harmonic generation

In order to verify the ferroelectric nature as well as the symmetry of the light induced super crystal, we

performed optical second harmonic generation (SHG) polarimetry analysis. Room temperature p/s-polarized SHG response at 400 nm from the super crystal were recorded as a function of the optical polarization direction of an 800 nm beam under normal incidence. The sample was oriented with the $[1\bar{1}0]_{DSO}$ direction along lab X-axis (horizontal), and $[001]_{DSO}$ direction along lab Y-axis (vertical) (see Fig. **S4**). The high-quality polarization dependent SHG signal revealed the ferroelectric nature of the super crystal, which can be modelled with both 4mm and mm2 point group symmetry with rotational axis in the sample plane (solid lines). Since the superlattice unit cell length scale (~20 nm) is much smaller than that of optical wavelength (400 and 800 nm), this large unit cell acts as an effective symmetry object for the SHG probe. Furthermore, the 4mm point group symmetry can be ruled out due to the in-plane 4-fold rotation operation is incompatible with the superlattice stacking structure. Therefore, SHG analysis revealed mm2 point group symmetry of the supercrystal structure, in support of the RSM observations of orthorhombic symmetry at the supercrystal cell level.

Topography and domain structure characterization

Piezo force microscopy and atomic force microscopy were performed at Pennsylvania State University (Bruker Icon I), at University of California, Berkeley (MFP-3D, Asylum Research), and at Center for Nanophase Materials Sciences, Oak Ridge National Laboratory (Cypher, Asylum).

Data Availability

Raw data from the Advanced Photon Source and phase field results are available upon reasonable request. The X-ray diffraction reciprocal space volumes generated with rsMap3D for figures both in the main text and supplement are available at (**To be determined**) together with python notebooks for interacting with the datasets. For non-python users, the data can be view with the paraview application available at www.paraview.org.

Author Contributions

V.A.S. conceived of the central concepts and designed the experiments. Together with H.W., J.W.F., N.L., Y.Y., Z.Z., M.R.M, D.A.W, A.R.D., J.K., X.Z., V.A.S. conducted the synchrotron-

based X-ray diffraction studies. C.D., Z.H., L.-Q.C. conducted the phase field modelling and analysis in collaboration with V.A.S. V.A.S, N.L., S.L., and A.R.D. conducted the scanning probe-based PFM measurements. Y.Y. and V.A.S. conducted the time-resolved SHG measurements. G.A.S. measured TEM to confirm sample quality. M.R.M., A.Y., S.D., R.R., and L.W.M. synthesized the materials. V.A.S., V.G., and J.W.F. wrote the manuscript with contributions from all authors. All authors discussed the results and implications of the work and read, edited and commented on the manuscript at all stages.

References

[1] Basov, D., Averitt, R. D., van der Marel, D., Dressel, M. & Haule, K. Electrodynamics of correlated electron materials. *Rev. Mod. Phys.* **83**, 471-541 (2011).

[2] Zhang, J. & Averitt, R. D. Dynamics and control in complex transition metal oxides. *Annu. Rev. Mater. Res.* **44**, 19-43 (2014).

[3] Giannetti, C., Capone, M., Fausti, D., Fabrizio, M., Parmigiani, F. & Mihailovic, D. Ultrafast optical spectroscopy of strongly correlated materials and high-temperature superconductors: a non-equilibrium approach. *Adv. Phys.* **65**, 58-238 (2016).

[4] Kirilyuk, A., Kimel, A. V. & Rasing, T. Ultrafast optical manipulation of magnetic order. *Rev. Mod. Phys.* **82**, 2731-2784 (2010).

[5] Fausti D. et al. Light-induced superconductivity in a stripe-ordered cuprate. *Science* **331**, 189-191 (2011).

[6] Torchinsky, D. H., Mahmood, F., Bollinger, A. T., Bozovic, I. & Gedik, N. Fluctuating charge-density waves in a cuprate superconductor. *Nat. Mater.* **12**, 387–391 (2013).

[7] Kim, K. W. et al., Ultrafast transient generation of spin-density-wave order in the normal state of $BaFe_2As_2$ driven by coherent lattice vibrations. *Nat. Mater.* **11**, 497–501 (2012).

[8] Wuttig, M. & Yamada, N. Phase-change materials for rewriteable data storage. *Nat. Mater.* **6**, 824-832 (2007).

[9] Ichikawa, H. et al. Transient photoinduced 'hidden' phase in a manganite. *Nat. Mater.* **10**, 101-105 (2011).

[10] Tao, Z. et al. The nature of photoinduced phase transition and metastable states in vanadium dioxide. *Sci. Rep.* 6, 38514 (2016).

[11] Stojchevska, L. et al. Ultrafast switching to a stable hidden quantum state in an electronic crystal. *Science* **344**, 177-180 (2014).

[12] Zhang, J. et al. Cooperative photoinduced metastable phase control in strained manganite films. *Nat. Mater.* **15**, 956-960 (2016).

[13] Aguado-Puente, P. & Junquera, J. Structural and energetic properties of domains in $PbTiO_3$/$SrTiO_3$ superlattices from first principles. *Phys. Rev. B* **85**, 184105 (2012).

[14] Yadav, A. K. et al. Observation of polar vortices in oxide superlattices. *Nature* **530**, 198–201 (2016).

[15] Hong, Z. et al. Stability of polar vortex lattice in ferroelectric superlattices. *Nano Lett*. 17, 2246-2252 (2017).

[16] Damodaran, A. R. et al. Phase coexistence and electric-field control of toroidal order in oxide superlattices. *Nat. Mater.* **16**, 1003-1009 (2017).

[17] Lu, L. et al. Topological defects with distinct dipole configurations in $PbTiO_3$-$SrTiO_3$ multilayer films. *Phys. Rev. Lett.* **12**, 177601 (2018).

[18] Laanait, N. et al. Full-field X-ray reflection microscopy of epitaxial thin-films. *J. Synchrotron Radiat.* **21**, 1252–1261 (2014).

[19] Laanait, N., Zhang, Z. & and Schlepütz, C. M. Imaging nanoscale lattice variations by machine learning of x-ray diffraction microscopy data. *Nanotechnology* **27**, 374002 (2016).

[20] Zelezny, V. et al. The variation of $PbTiO_3$ bandgap at ferroelectric phase transition, *J. Phys.-Condens. Matter* **28**, 025501 (2016).

[21] Daranciang, D. et al. Ultrafast photovoltaic response in ferroelectric nanolayers. *Phys. Rev. Lett.* **108**, 087601 (2012).

[22] Ahn, Y. et al. Photoinduced Domain pattern transformation in ferroelectric-dielectric superlattices. *Phys. Rev. Lett.* **119**, 057601 (2017).

[23] Schafranek, R., Li, S., Chen, F., Wu, W., and Klein, A., $PbTiO_3/SrTiO_3$ interface: Energy band alignment and its relation to the limits of Fermi level variation, Phys Rev B **84**, 045317 (2011).

[24] Torres-Pardo, A., et. al., Spectroscopic mapping of local structural distortions in ferroelectric $PbTiO_3/SrTiO_3$ superlattices at the unit-cell scale, Phys Rev B **84**, 220102 (2011).

[25] Hasegawa, T., Mouri, S.-I., Yamada, Y. and Tanaka, K. Giant Photo-Induced Dielectricity in $SrTiO_3$, J Phys Soc Jpn **72**, 41 (2003).

[26] Nasu, K. Photogeneration of superparaelectric large polarons in dielectrics with soft anharmonic $T1u$ phonons, Phys Rev B **67**, 174111 (2003).

[27] Mehta, R.R., Silverman, B.D., and Jacobs, J.T., Depolarization fields in thin ferroelectric films, J. Appl. Phys. **44**, 3379 (2003).

[28] Kim, D.-J., Jo, J. Y., Kim, Y.S., Chang, Y. J., Lee, J. S., Yoon, J. G. , Song, T. K., and Noh, T. W., Polarization Relaxation Induced by a Depolarization Field in Ultrathin Ferroelectric $BaTiO_3$ Capacitors, Phys. Rev. Lett. **95**, 237602 (2005).

[29] Chen, L.-Q. Phase-field method of phase transitions/domain structures in ferroelectric thin films: A review. *J. Am. Ceram. Soc.* **91**, 1835-1844 (2008).

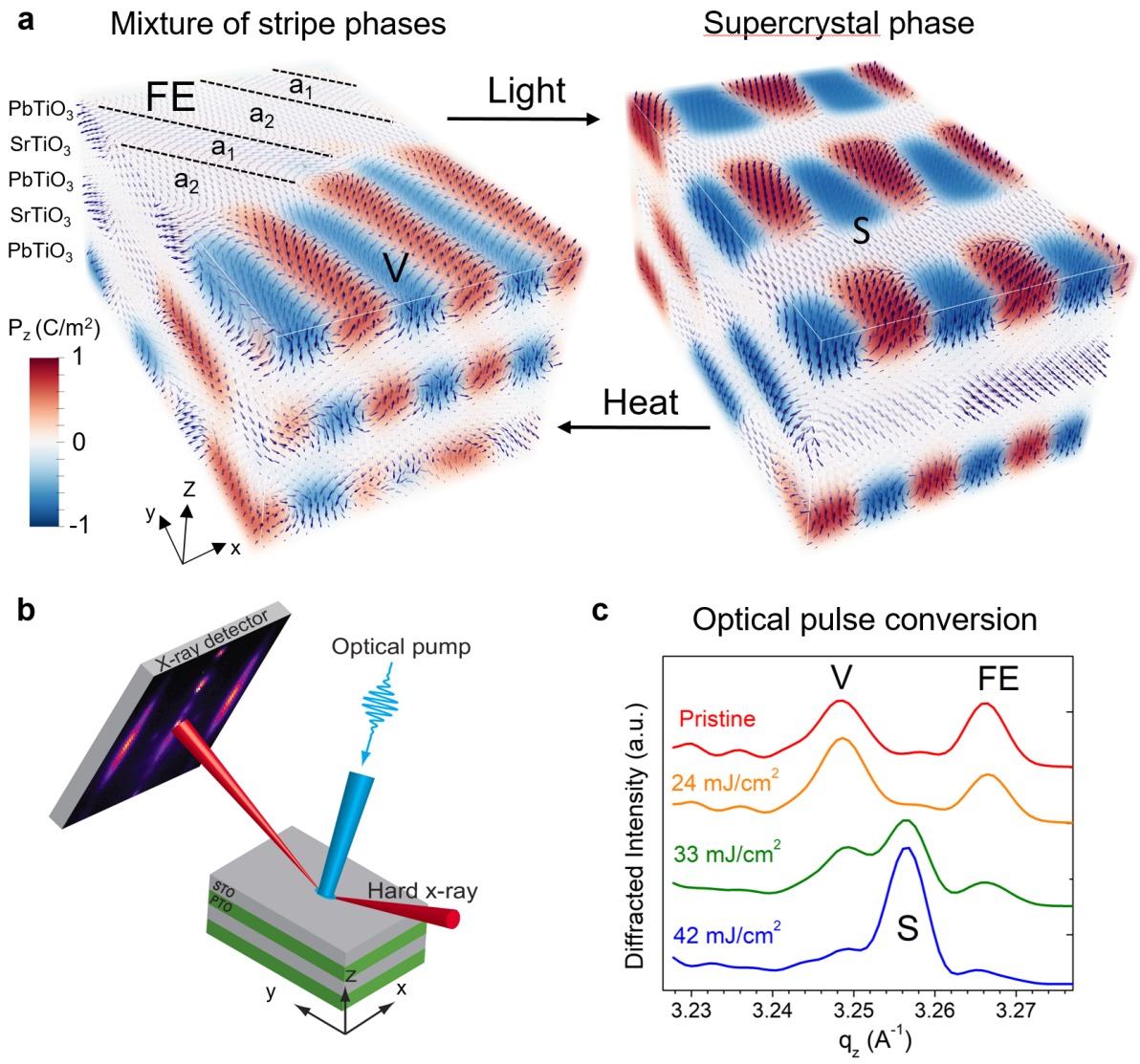

Figure 1 | **Summary of the supercrystal formation: a.** A two-phase mixture of in-plane ferroelectric-ferroelastic a_1/a_2 domains (**FE**) and polar vortex (**V**) is converted to a single 3-D supercrystal (**S**) phase by sub-ps optical pulses in a $PbTiO_3/SrTiO_3$ superlattice. The S-phase contains ferroelectric, ferroelastic and polar vortex sub-regions ordered in 3-D. Thermal annealing reverses this transition. The arrows inside panel **a** indicates the local polar displacements obtained from a phase-field model. The red and blue color contrasts illustrate the up and down z-component of the polarization (P_z). The white regions correspond to in-plane polarization. **b.** The 400nm wavelength optical-pump, X-ray diffraction probe study configuration. The real space directions are aligned with reciprocal space and substrate crystallographic directions in the following way: x || H || [001], y || K || [-110], and z || L || [110]. **c.** Superlattice peaks near 002_{pc} showing two distinct diffraction peaks, corresponding to the V and FE phases in the pristine sample that transform into a single uniform S-phase with single-shot optical excitation above a certain threshold energy density.

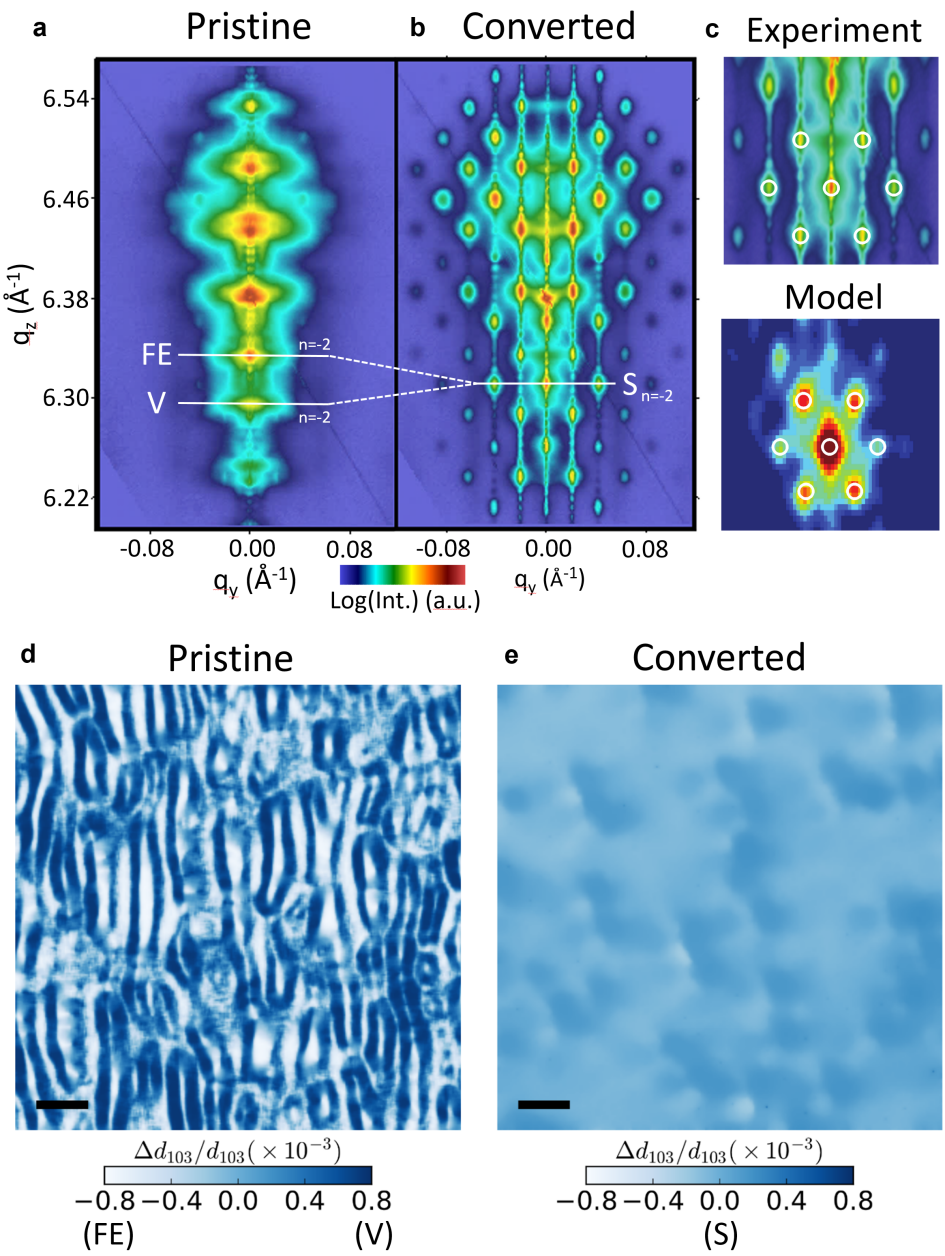

Figure 2 | Supercrystal observation by X-ray diffraction and microscopy: a. Diffraction along the K-L (q_y-q_z) plane for the mixed phase (FE + V) pristine sample shows evidence of order only along the z direction with distinct peaks due to the FE and V phases, as noted by the horizontal lines. **b.** Upon optical excitation with light above the PTO bandgap, a periodic 2-dimensional diffraction pattern appears due to spatial ordering in the y-z plane. **c.** The experimental diffraction pattern of S-phase is in good agreement with a Fast Fourier transform of the real space structure from the phase field model. **d.** Diffraction microscopy of the pristine phase shows a large mesoscale strain variation due to the mixture of FE (light) and V (dark) phases. **e.** With the formation of the supercrystal phase, the strain variation is strongly reduced and the image contrast becomes uniform on the mesoscale. The scale bars in **c** and **d** are 500 nm.

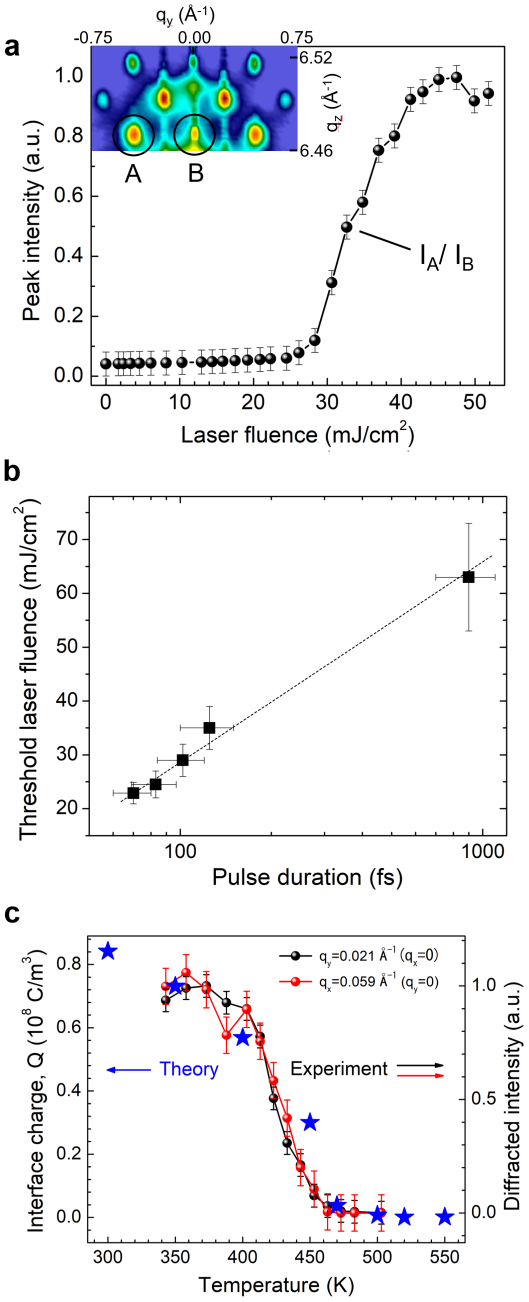

Figure 3 | Reversible control of supercrystal phase formation: a. Laser fluence dependence of S-phase formation determined from the in-plane S-phase reflection (I_A) normalized to the specular peak (I_B) following a multi-shot exposure (~ 500 shots) to ~ 80 fs optical pulses, showing a critical fluence of ~ 25 mJ/cm^2. Inset is the corresponding K-L diffraction pattern near 004_{pc}. **b.** The variation of laser fluence threshold with pulse duration at 300 K extracted from normalized intensity changes of the in-plane ordering peak of S-phase, as shown in **a**. **c**. (Right) Temperature dependence of in-plane S-phase ordering peaks along the H and K directions (red and black dots), which shows stability near room temperature and the abrupt disappearance of the S-phase at high temperature. (Left) Comparison with temperature dependent calculations of the interfacial charge density from phase field modeling (blue stars).

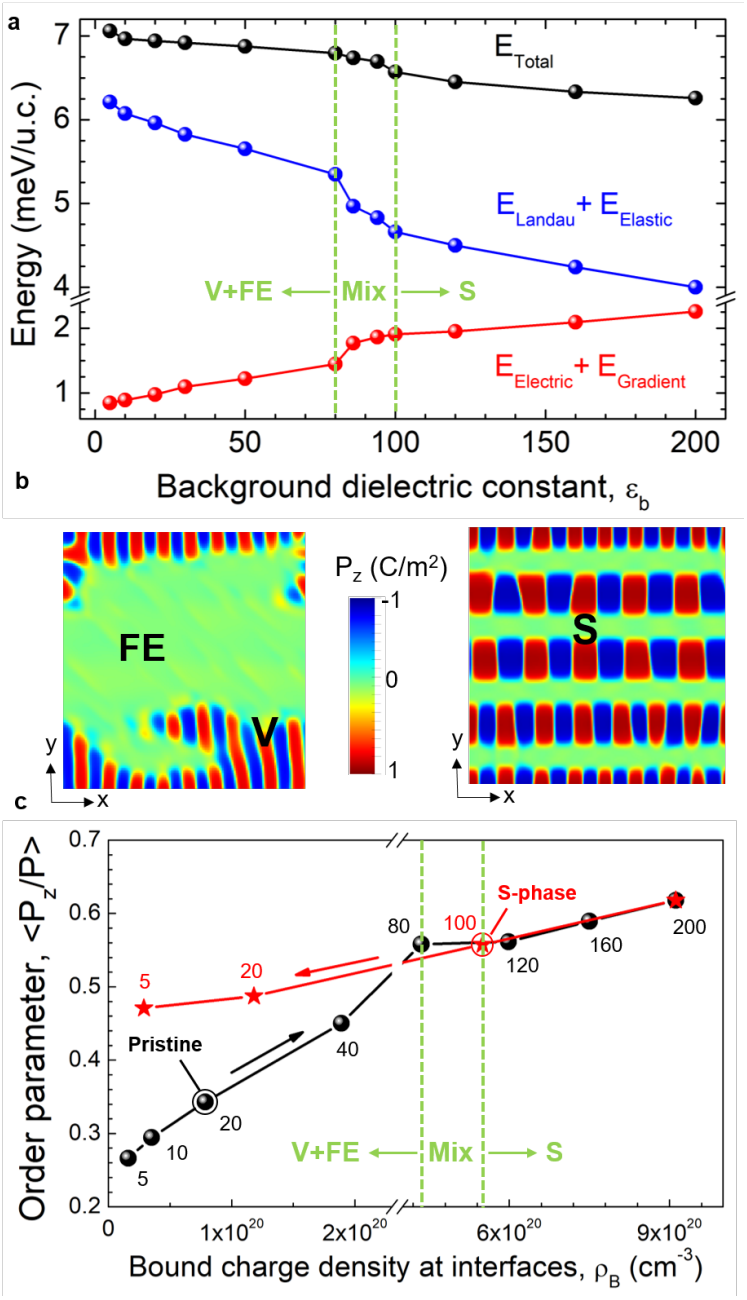

Figure 4 | Phase field model prediction of the supercrystal phase: **a.** Energy evolution versus background dielectric constant, ε_b, showing the evolution of the 4 terms in the free energy for $\varepsilon_b < 80$, where energy increase for electric and gradient energy are compensated by Landau and elastic contributions to the total energy. For ε_b between 80 and 100, all energy contributions change more abruptly, marking the transition to the S-phase, followed by recovery of relatively slower changes at $\varepsilon_b > 100$ after S-phase formation is completed. **b.** Vertical component of polarization spatial distributions at ε_b values below and above the threshold. **c.** Phase diagram showing the evolution of P_z inside a PTO layer plotted versus the bound charge density, ρ_B, at the interface between PTO and STO, which correlates with the background dielectric constant, ε_b (values noted on plot). On increasing ε_b, there is a transition from FE+V to S at a threshold $\varepsilon_b = 80$ and the S-phase remains for values above this level (black dots). The subsequent relaxation of ε_b back to lower values (red points), shows the S-phase ordering remains quasi-stable even below the threshold value.

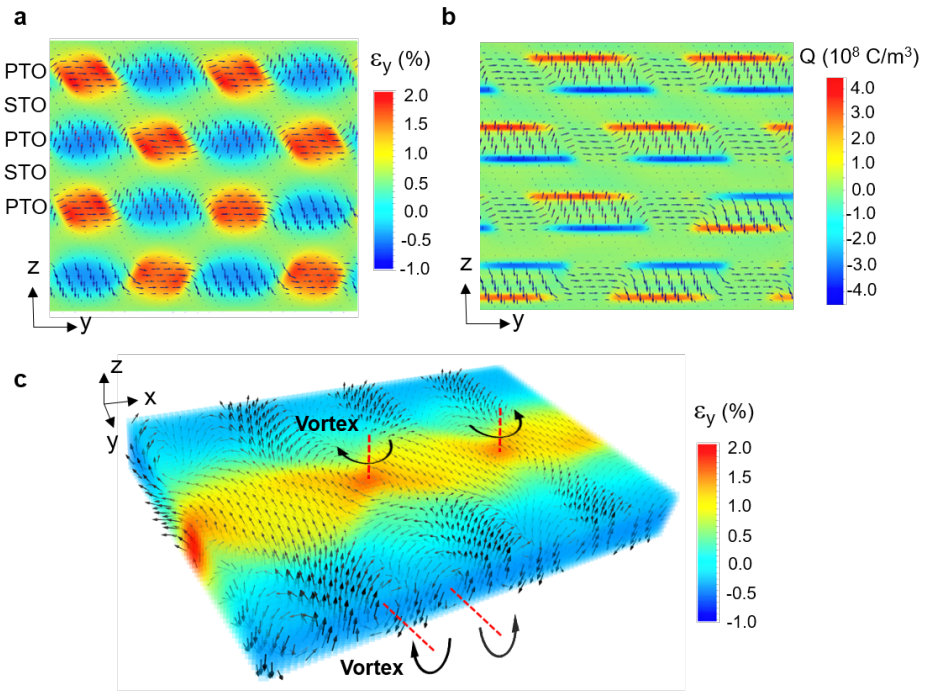

Figure 5 | Interplay between order parameters within the supercrystal phase captured by phase field model: The spatially correlated ordering of **a.** In-plane strain distribution and **b.** corresponding bound charge distribution that are overlaid with polar displacement vector maps inside a selected *y*-*z* plane of the superlattice. The horizontally polarized regions from adjacent PTO layers interact elastically and electrically through the STO layer, which creates an antiphase stacking as the most stable configuration. **c.** A 3-D view of a representative PTO layer where in-plane strain (ε_y) distribution is overlaid with polar displacement vector maps. Along the *x*-*y* plane, the polar vortex order alternates between in-plane and out-of-plane orientation for their respective vortex axes.